

## Article

# Boosting the Power of $\text{Na}_{0.44}\text{MnO}_2$ : Unlocking Its Potential for Aqueous Sodium-Ion Storage through Nanostructuring and Hybridization

Mehdi Soleimanzade <sup>1</sup>, Mariano Radaelli <sup>1</sup>, Jacopo Manidi <sup>2</sup>, Maksim Bahdanchyk <sup>2</sup> and Antonello Vicenzo <sup>2,\*</sup>

<sup>1</sup> Ricerca Sul Sistema Energetico—RSE S.p.A., via Raffaele Rubattino 54, 20134 Milano, Italy; mehdi.soleimanzade@rse-web.it (M.S.); mariano.radaelli@rse-web.it (M.R.)

<sup>2</sup> Dipartimento di Chimica, Materiali e Ingegneria Chimica “Giulio Natta”, Politecnico di Milano, Via Luigi Mancinelli 7, 20131 Milano, Italy; jacopo.manidi@polimi.it (J.M.); maksim.bahdanchyk@polimi.it (M.B.)

\* Correspondence: antonello.vicenzo@polimi.it; Tel.: +39-2-23993140

**Abstract:** We report an effective processing route, combining nanostructure formation and hybridization, to improve the rate performance of the tunnel-structure sodium manganese oxide  $\text{Na}_{0.44}\text{MnO}_2$  (NMO) as a cathode material for aqueous sodium ion storage. We use hydrothermal synthesis to prepare an NMO/CNF (Carbon NanoFiber) hybrid, consisting of uniform oxide nanowires with an average width of 70 nm and length in the range of several tenths of  $\mu\text{m}$ . The highly dispersed CNFs impart high conductivity to the NMO/CNF electrode, allowing high-rate performance at a C-rate of up to 20 C, with a delivered capacity of more than half the theoretical value in a 1 M  $\text{Na}_2\text{SO}_4$  electrolyte. Moreover, the NMO/CNF hybrid shows good electrochemical stability under several hundred cycles at a high C-rate. However, the NMO nanowire electrodes reveal a lower-than-expected capacity, probably as a result of the tendency of nanowires to form bundles, which prevents direct contact with conductive fibers and induce the under-utilization of active material. With this study, we demonstrate a strong improvement of the otherwise inherently low-rate performance of NMO through oxide nanostructuring and hybridization with carbon fibers, paving the way for further research on NMO-based materials for aqueous sodium ion storage.



**Citation:** Soleimanzade, M.; Radaelli, M.; Manidi, J.; Bahdanchyk, M.; Vicenzo, A. Boosting the Power of  $\text{Na}_{0.44}\text{MnO}_2$ : Unlocking Its Potential for Aqueous Sodium-Ion Storage through Nanostructuring and Hybridization. *Batteries* **2023**, *9*, 428. <https://doi.org/10.3390/batteries9080428>

Academic Editor: Xianyong Wu

Received: 5 July 2023

Revised: 18 July 2023

Accepted: 14 August 2023

Published: 17 August 2023



**Copyright:** © 2023 by the authors. Licensee MDPI, Basel, Switzerland. This article is an open access article distributed under the terms and conditions of the Creative Commons Attribution (CC BY) license (<https://creativecommons.org/licenses/by/4.0/>).

## 1. Introduction

Aqueous sodium-ion batteries (ASIB) are regarded as a feasible technology for grid-scale energy storage due to their low cost, safety and environmental acceptance [1,2]. Similarly to other aqueous rechargeable batteries, essential concerns about ASIB technology pertain to the stability of active materials and the limitation of the operating voltage in aqueous environments [1,3]. Nonetheless, while these concerns impose strong constraints on the choice of electrode materials [4] and stimulate research on novel electrolytes [3], the primary objectives remain to select and develop Na-ion insertion materials with characteristics enabling the practical use of ASIBs [4]. Undoubtedly, to ensure a low environmental impact, the use of toxic elements, such as Co, V, or Ni, should be avoided [5], and preference should be given to sustainable processes of synthesis [6]. In this regard, Mn-based cathode materials are probably the least harmful solution; in addition, they have been widely used and studied in much detail—particularly in the case of Mn-based oxides—as cathodes of aqueous storage devices, ranging from asymmetric supercapacitors [7] to aqueous metal-ion batteries [8]. Indeed, the wealth of knowledge and depth of understanding of this class of materials are hardly matched by those of other materials being studied as cathodes for future aqueous batteries. Still, Mn-based oxides present intrinsic limitations and critical

aspects, specifically poor electronic conductivity [9,10], proneness to dissolution and re-deposition—see, e.g., [11]—and the Jahn–Teller distortion of Mn(III) [12], that call for a careful assessment of the conditions enabling their implementation in aqueous storage devices. In relatively more recent times, tunnel-type sodium manganese oxides (tt-NMO) [13] have emerged as potential candidate cathode materials for aqueous electrolyte batteries [8] and for aqueous electrolyte hybrid cells [14]. The distinct quality of this material family—most notably of the prototype compound  $\text{Na}_{0.44}\text{MnO}_2$  (NMO) [14]—is the promise of great stability in aqueous electrolytes, at the cost, however, of a low specific capacity, due to the limited range over which the sodium content can be varied [15], as dictated by the need to preserve structural integrity [16] and prevent oxide dissolution [15,17]. However, with the current state of research, tt-NMO materials appear as a more reasonable choice than do layered structure sodium manganese oxides, which—while providing a larger specific capacity—are inherently prone to structural deformations, compromising cycle life and leading eventually to structural instabilities [4,18,19]. Still, with regard to the specific capacity limitation of NMO, it is worth remarking that while safety, low operation maintenance costs, and cycle life are primary requirements [20], stationary energy storage applications have a degree of tolerance for relatively low energy densities, having no tight constraints on weight and volume, not to mention the different requirements of the wide and diverse range of application markets [21]. Furthermore, thick electrodes are a practical solution with which to compensate for low energy density, as long as improved rate capability can be achieved to allow for a good power response—which is instead a desirable property of the storage system [21].

Overall, notwithstanding its limited capacity,  $\text{Na}_{0.44}\text{MnO}_2$  has received much attention as a prospective cathode material for Na-ion storage systems [2–4,22], and remains a model system for the investigation of possible strategies for the enhancement of the performances of tt-NMO materials in ASIBs [13,15]. The unique structure of NMO—which crystallizes in the orthorhombic lattice, Pbnm space group [23]—is characterized by the arrangement of  $\text{MnO}_6$  octahedra and  $\text{MnO}_5$  square pyramids forming a double-tunnel structure, with large S-shaped channels that allow for Na ion transport along the [001] direction of the unit cell [16,24]. It is the tunnel structure that accounts for structural stability during the cycling of NMO [14,25] compared to its  $\text{Na}_x\text{MnO}_2$  layered-structure counterpart, as shown in early studies [26], and as widely reported in the current literature, e.g., in [13,27]. Possibly, a more controversial issue in the search for the better performance of NMO is rate capability, being a system characteristic affected by material factors as well as by design aspects of an electrode and cell. In this regard, while the rate capability of NMO electrodes can be improved substantially in aqueous vs. organic electrolytes [28]—thanks to the increase of several orders of magnitude in the apparent diffusion coefficient [15,28]—rate performance is still severely limited by the intrinsic low conductivity of the oxide, pointing to the need to resort to multiple strategies for performance enhancement [29], such as reducing the size of the active material, tuning the particle morphology and forming a composite. The formation of nanostructures—a method that has had a great impact on the development of battery cathode material research [29,30]—has been widely explored for non-aqueous SIBs [31] and a number of different methods of synthesis were reported for this purpose; see [31,32] and the references therein. Specifically, NMO nanowires were obtained via the hydrothermal conversion of birnessite [33,34] and their application was demonstrated in non-aqueous lithium [35] and sodium [36] batteries. However, the combination of a nanoscale structure and the control of the particle morphology of tt-NMO has not been fully exploited in the context of ASIBs. Composite formation, on the other hand, is a design option that can be hardly ignored when dealing with oxides as active materials. While a recourse to carbon coating [37]—a very effective method to reduce inter-particle resistance—is not a viable solution for manganese oxides, for their susceptibility to reduction under C-coating processing conditions, there are several studies reporting the improvement of the rate capability of composite electrodes of either tunnel- or layered-structure sodium manganese

oxides, mostly with carbon nanotubes, both in organic [38] and aqueous electrolytes [39–42], and with polypyrrole, in organic electrolytes [43,44].

In this study, we resort to a combination of nanostructuring and hybridization with a conductive nanoscale material, carbon nanofibers (CNFs), to boost the rate capability of NMO, by focusing on reducing both the ionic and electron transport resistance. Diverging from the reported hydrothermal synthesis of NMO nanowires [33,35], we show that it is possible to obtain an NMO nanowire/CNF hybrid via hydrothermal synthesis in a strong NaOH solution using  $\text{MnO}_2$  as the manganese precursor, instead of  $\text{Mn}_3\text{O}_4$  [35] or  $\text{Mn}_2\text{O}_3$  [33], and CNFs as the disperse nanoscale conductive phase. Electrodes based on the NMO/CNF hybrid have an excellent rate capability, delivering more than half the theoretical capacity at a 20 C rate, and promising cycle performance, retaining an almost constant discharge capacity at a high C rate over a hundred cycles.

## 2. Materials and Methods

### 2.1. Hydrothermal Synthesis

Sodium hydroxide (Carlo Erba, >97%), manganese (III) oxide,  $\text{Mn}_2\text{O}_3$ , and manganese dioxide,  $\text{MnO}_2$  (Sigma-Aldrich, St. Louis, MO, USA, ≥99.5%), were used as the reagents in the hydrothermal synthesis of NMO nanowires and the NMO nanowires/CNF hybrid, respectively. Carbon nanofibers, CNFs, were purchased from Sigma-Aldrich (graphitized and iron-free; diameter × length: 100 nm × 20–200  $\mu\text{m}$ ). The reaction was performed in an autoclave consisting of a 30 mL polytetrafluoroethylene liner and a stainless-steel vessel. The solids were first mixed in 10 M NaOH and kept under stirring for about 1 h at room temperature. The liner was filled with the solution, leaving a 25% empty volume, closed and sealed in the autoclave vessel and heated in a muffle furnace to the target temperature of 206 °C within 60 min. The step sequence and holding time depended on the manganese precursor, i.e., on the desired product, NMO or NMO/CNF; in any case, the holding time was prolonged by six hours for equilibrating the temperature inside the reactor. For the synthesis of NMO nanowires from the  $\text{Mn}_2\text{O}_3$  precursor, the hydrothermal process consisted of three steps, each lasting for a 24 h duration; i.e., the treatment was discontinued; the reaction vessel was cooled down to room temperature and opened; the solid was recovered and then dispersed again in a 10 M NaOH solution to resume the treatment. As shown in the following (Section 3.1.1), segmentation is essential to the transformation of birnessite in NMO, allowing for the supply of the oxygen needed to sustain manganese oxidation. The preparation of the NMO/CNF hybrid from the  $\text{MnO}_2$  precursor was performed in a single step of 24 h treatment. Upon completion of the hydrothermal process, the products were washed with deionized water and separated via centrifugation repeatedly until the pH of the washing solution was roughly neutral. Prior to characterization and electrode fabrication, the NMO samples were dried overnight in a vacuum furnace at 60 °C to eliminate residual moisture.

### 2.2. Microstructure and Physical Characterization

The NMO samples were analyzed for phase structure via X-ray diffraction (XRD), using a Bruker D2 Phaser diffractometer operated in the Bragg–Brentano geometry, with a step size of 0.02° and a dwell time of 38 s. XRD patterns of the samples were analyzed via the Rietveld refinement method for the calculation of lattice parameters and the evaluation of phase composition. The NMO and birnessite phases were indexed as  $\text{Na}_{0.44}\text{MnO}_2$  (JCPDS 04-018-3147 [45]) and  $\text{Na}_{0.55}\text{Mn}_2\text{O}_4 \cdot 1.5\text{H}_2\text{O}$  (JCPDS 00-043-1456), respectively. The Rietveld refinement of the crystal structure was performed by using TOPAS software [46]. Difference profile plots and agreement indices are provided as a visual and numerical description of the fit of the calculated pattern to the observed data, respectively. The following indices were used [47]: the weighted-profile R-factor,  $R_{wp}$ , the unweighted-profile R-factor,  $R_p$ , the statistically expected R value,  $R_e$ , and the goodness-of-fit indicator,  $S = R_{wp}/R_e$ . Samples were analyzed via transmission electron microscopy (TEM), using a Philips CM200 FEG microscope, equipped with a Schottky emitter field emission gun operated at 200 kV, and

via scanning electron microscopy (SEM) using Tescan Mira 3 Field Emission SEM (FESEM) operated at 20 kV. The evaluation of the specific surface area was performed using the Brunauer–Emmett–Teller (BET) method applied to N<sub>2</sub> adsorption/desorption isotherms measured with an Autosorb iQ gas sorption system (Quantachrome Instruments). Raman spectra were obtained with Horiba Scientific Raman Spectrometer (XploRA™ PLUS). The electrical conductivity of sample powders compacted under pressure was measured using a lab-made setup, as reported previously [48,49].

### 2.3. Electrode Fabrication

We used a paste method for the fabrication of electrodes, as described previously [50]. The NMO nanowire electrodes consisted of the active material with PTFE (Sigma-Aldrich, 60 wt% dispersion in H<sub>2</sub>O) serving as the binder and conductive carbon (CC, TIMCAL C-NERGY™ SUPER C65) to enhance conductivity, using an NMO:CC:PTFE ratio of 70:22:8. After rolling the paste using a roll press machine (TOB), a thin, self-supporting sheet, of approximately 100 μm in thickness was obtained. From this sheet, electrodes with a geometric area of 1 cm<sup>2</sup> and an areal mass loading of 15.0 ( $\pm 2.2$ ) mg cm<sup>-2</sup> were cut. These electrodes were then stuck to a graphite foil current collector with a conductive adhesive (E-dag®). The NMO nanowire/CNF hybrid electrodes were prepared with the same procedure, using a paste composed of 92 wt% of NMO/CNF powder and 8 wt% of PTFE binder, i.e., without the addition of CC.

### 2.4. Electrochemical Characterization

All electrochemical measurements—galvanostatic charge and discharge cycling (GCD), cyclic voltammetry (CV), and electrochemical impedance spectroscopy (EIS)—were performed using a Biologic model VMP3 instrument. A three-electrode experimental setup was used, with the NMO electrode serving as the working electrode, a platinum foil serving as the counter electrode, and a calomel reference electrode (KCl 3.5 M, +0.250 V vs. SHE) serving as the reference. Throughout the manuscript, potential is expressed vs. SHE for ease of reference. All tests were conducted at room temperature in an aqueous 1 M Na<sub>2</sub>SO<sub>4</sub> electrolyte at a pH of about 7. For CV analysis, 5 successive cycles, over the potential range from 0.25 to 1.0 V vs. SHE, were performed at a scan rate of 0.2 mV s<sup>-1</sup>. EIS measurements were performed at the open-circuit potential (OCP) using a perturbation signal of a 10 mV rms amplitude over the frequency range of 300 kHz to 5 mHz, sampling 10 points per decade. The Boukamp method was used to check the Kronig–Kramers compliance of the EIS data [51].

## 3. Results and Discussion

### 3.1. Hydrothermal Synthesis

In the hydrothermal synthesis of NMO nanowires and the NMO nanowire/CNF hybrid, we used Mn<sub>2</sub>O<sub>3</sub> and MnO<sub>2</sub> as the manganese precursor, respectively. The hydrothermal formation of NMO nanowires occurs through the intermediate crystallization of birnessite nanosheets [33] via an exfoliation process in which Na ions intercalate into the MnO<sub>6</sub> or MnO<sub>5</sub> building block of manganese oxides [34]. The type of manganese precursor determines to a large extent the composition of the product mixture and the kinetics of conversion [52]. Given the limited availability of oxygen in the reaction mixture, to maximize the yield in NMO within a reasonable time of treatment, the oxidation state of Mn in the precursor should preferably be as close as possible to the average oxidation state of 3.56 in NMO. This is the reason why the Mn(III) oxide was used for the hydrothermal synthesis of NMO. On the other hand, the presence of CNFs in the reaction mixture imposed a reducing environment and required the use of MnO<sub>2</sub> as the precursor. In either case, the reaction medium was a 10 M aqueous solution of NaOH.

In the following, we give a short account of the synthesis of NMO nanowires to illustrate the experimental background that has been used for defining test conditions for the obtainment of the desired products. Table 1 summarizes the test conditions of the

hydrothermal synthesis performed and reports the results of the quantitative Rietveld analysis of the phase composition of the samples.

**Table 1.** Hydrothermal synthesis of NMO nanowires and NMO nanowires/CNF hybrid; test conditions and quantitative analysis of crystal phases (wt%).

Test/Sample	Precursor	Time (Day)	Quantitative Analysis (wt%)			
			Mn <sub>3</sub> O <sub>4</sub>	Birnessite	NMO	C
HT#1	Mn <sub>2</sub> O <sub>3</sub>	1	57	22	21	-
HT#2	(*)	1	11	16	73	-
HT#3/H-NMO -/NMO/CNF	(*) MnO <sub>2</sub> + 30%CNF	1	-	1.5	98.5	-
			-	2.8	77.9	19.3

(\*) After HT#1 (24 h), the hydrothermal reaction was interrupted; it was resumed with HT#2 (24 h) and, after another interruption, with HT#3 (24 h) to obtain the final product. At each step, the 10 M NaOH solution was renewed.

### 3.1.1. NMO Nanowires

The initial black powder of pure Mn<sub>2</sub>O<sub>3</sub> transformed into entangled brownish cloth-like NMO over the course of 3 days, through three steps of reaction lasting 24 h each; see Table 1. After 24 h (HT#1), Mn<sub>2</sub>O<sub>3</sub> transformed into a mixture of 22% birnessite (Na<sub>0.55</sub>Mn<sub>2</sub>O<sub>4</sub>·1.5H<sub>2</sub>O), 57% Mn<sub>3</sub>O<sub>4</sub>, and 21% NMO (see Figure S1). The SEM image of Figure 1b (HT#1) shows a thorough modification of the morphology of pure Mn<sub>2</sub>O<sub>3</sub> (Figure 1a) and confirms the formation of ultra-long whiskers of NMO (indicated by the yellow arrow). Upon repetition of the treatment for another day—HT#2 in Table 1—the percentage fraction of NMO increased to 71%, implying the conversion of Mn<sub>3</sub>O<sub>4</sub> and birnessite into NMO (Figure S2); the larger population of NMO nanowires, along with birnessite nanosheets, is evident in Figure 1c. Eventually, upon resuming the hydrothermal treatment of the product of HT#2 for a further 24 h—HT#3 in Table 1—(Figure 1d), the product consisted of NMO nanowires with a percentage fraction of 98.5%, as derived from the Rietveld analysis of the XRD pattern in Figure 2a. The product of HT#3 will be referred to in the following as the sample H-NMO.

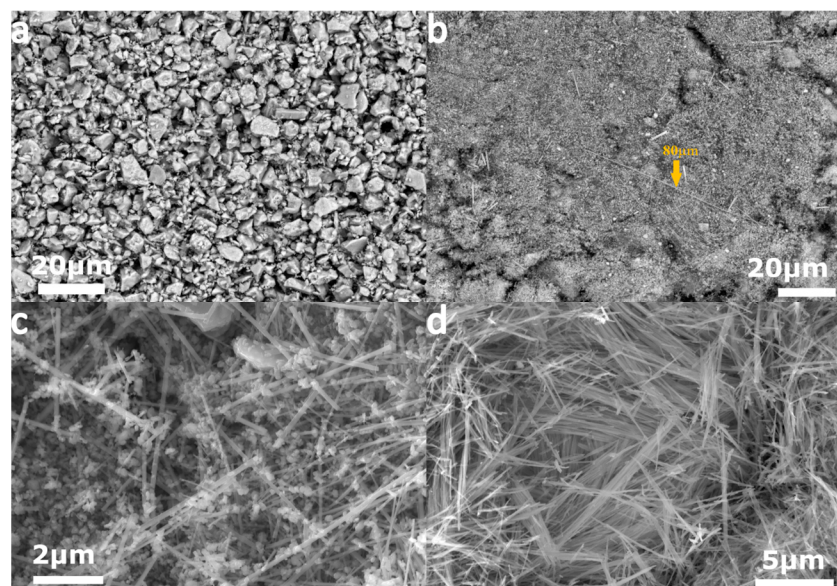


**Figure 1.** (a) Backscatter SEM image of Mn<sub>2</sub>O<sub>3</sub> reagent powder, (b) backscatter SEM image of the hydrothermal product of HT#1 (the yellow arrow indicates a NMO nanowire of about 80  $\mu$ m length), (c) secondary SEM image of the product of HT#2, and (d) of HT#3 (H-NMO sample).

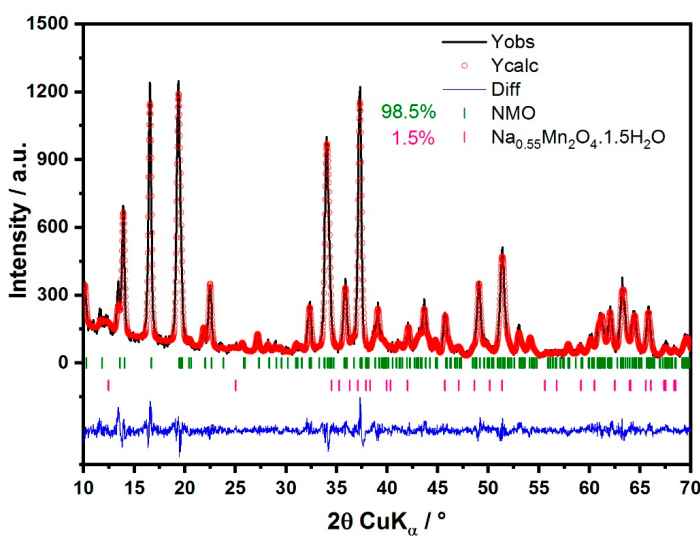


**Figure 2.** XRD pattern (black line) and Rietveld refinement (red dot symbols) of the product of hydrothermal treatment HT#3, sample H-NMO (Table 1); the graph below (blue line) shows the discrepancy; R values:  $R_{wp} = 10.08\%$ ;  $R_p = 7.55\%$ ; goodness of fit:  $S = 1.21$ .

As shown in Figure 1d, the nanowires had variable lengths, mostly in the range of a few tenths of micrometers, and a thickness of about 70 nm; moreover, the nanowires appeared to cluster in bundles of a similar size, about 1  $\mu$ m. The crystallinity of the NMO and the nanowire length were also evaluated via high-resolution TEM, as shown by the sample images in Figure 3; the nanowire length was confirmed to be in the range of a few tenths of  $\mu$ m, resulting in a varying aspect ratio of up to several hundred. The surface area of H-NMO was determined via BET analysis (see Figures S3 and S4 and Table S1) and found to be  $21.71 \text{ m}^2 \text{ g}^{-1}$ , i.e., about 15 times larger than that for NMO synthesized via a conventional solid-state reaction with a micro-rod morphology, which was  $1.5 \text{ m}^2 \text{ g}^{-1}$  [15]. The high-resolution TEM image in Figure 3b confirms the high crystallinity of the nanowires, with a lattice spacing of 0.86 nm corresponding to that of (110) crystal planes [53], in agreement with previous work [36]. The growth direction of the nanowires could be [001] or [110], but, due to the small thickness of the nanowires, it was not possible to obtain a well-resolved selected-area electron diffraction pattern. Still, following [33], the growth of NMO nanowires is likely to occur along the [001] crystal direction, as a result of the stress-mediated splitting of birnessite nanosheets, involving a topotactic mechanism where the [002] orientation of the final NMO phase ( $d_{002} = 1.41 \text{ \AA}$ ) is aligned with either the [020] or [110] orientation of the intermediate birnessite phase ( $d_{020} = 1.42 \text{ \AA}$ ).

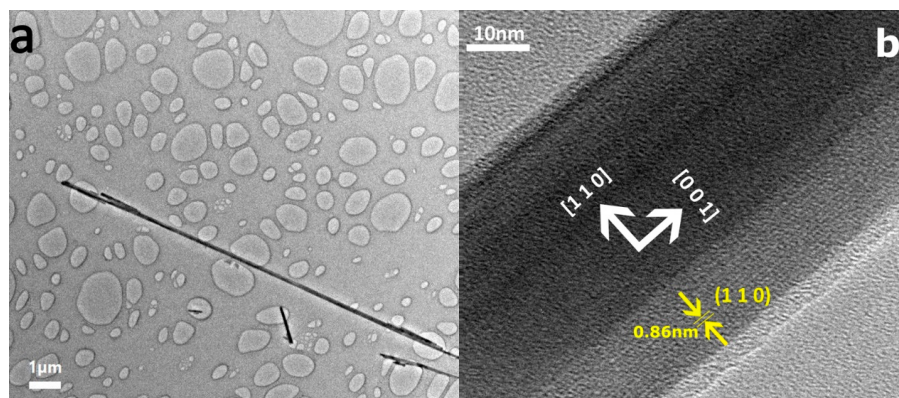
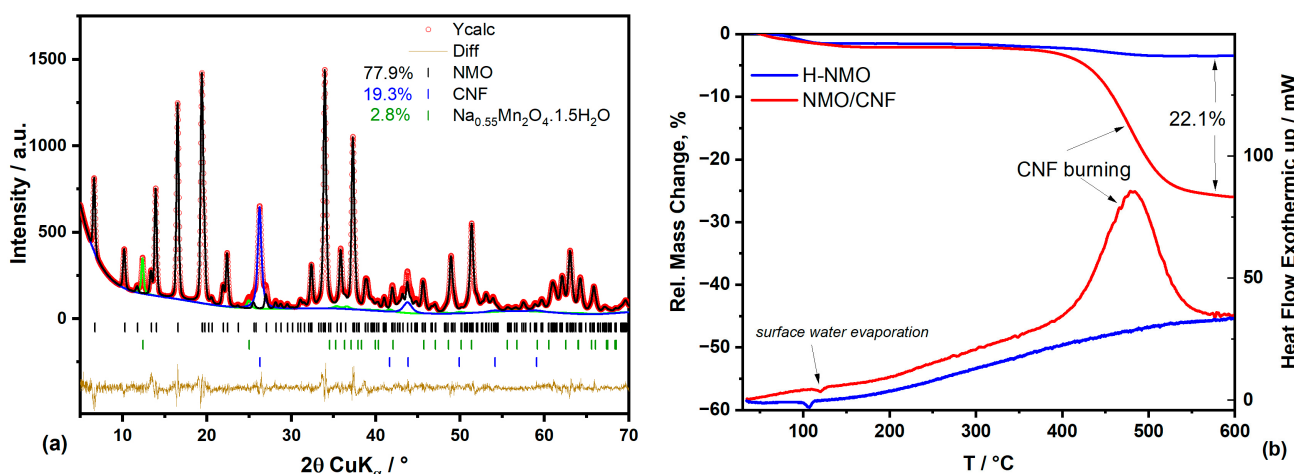


**Figure 3.** TEM images of H-NMO sample: (a) Bright-field TEM image of some NMO nanowires on glassy carbon and (b) high-resolution TEM image of the NMO nanowire with an indication of the crystal orientation.

Based on the evolution of the phases during the hydrothermal synthesis of NMO from  $\text{Mn}_2\text{O}_3$ , it is inferred that the  $\text{Mn}^{3+}$  (from  $\text{Mn}_2\text{O}_3$ ) must, first, undergo the disproportionation reaction  $2\text{Mn}^{3+} \rightarrow \text{Mn}^{2+} + \text{Mn}^{4+}$ , to account for the simultaneous formation of  $\text{Mn}_3\text{O}_4$  and birnessite. Indeed,  $\text{Mn}^{3+}$  transforms readily via dismutation into  $\text{Mn}^{2+}$  and  $\text{MnO}_2$  under alkaline conditions, as reported by Davies [54]. Furthermore, the conversion of birnessite into tunnel-structure oxides is believed to commence with the disproportionation of neighboring  $\text{Mn}^{3+}$  ions [55–57], followed by the migration of  $\text{Mn}^{2+}$  ions into interlayer gaps, where they are oxidized to  $\text{Mn}^{3+}$  by oxygen in the autoclave, thus facilitating the formation of  $\text{MnO}_6$  octahedra. In this regard, it is worth pointing out once again that, after each step of reaction (of 24 h), the autoclave was cooled down to room temperature and opened, to replenish the air in the liner headspace, in addition to allowing the sampling of the products at the various stages of reaction. We also remark that the role of oxygen in NMO formation is further proven by the fact that the relative amount and crystallinity of the NMO formed during HT#1 remained almost unaltered upon an increase in the (continuous) treatment time from 1 day to 6 days (Figure S3) [52].

### 3.1.2. NMO Nanowire/CNF Hybrid

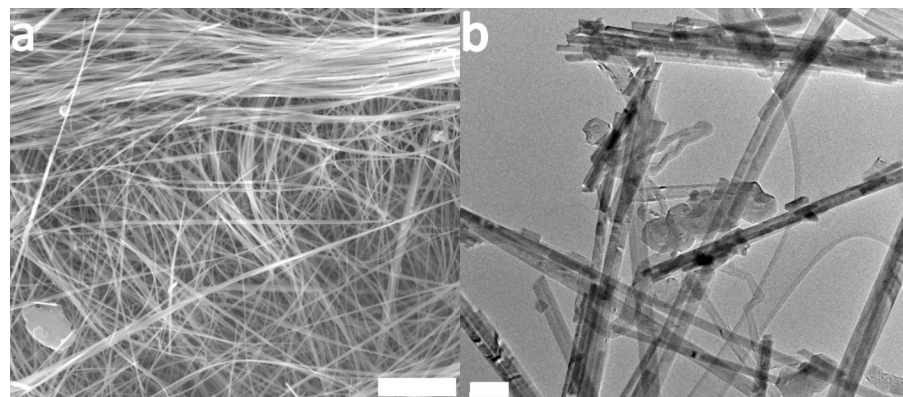
The requirement of slightly oxidizing conditions for the hydrothermal conversion of  $\text{Mn}_2\text{O}_3$  into NMO nanowires precludes the possibility to perform a hydrothermal process in the presence of graphitic carbon. In principle, the alternative precursor should have a higher oxidation state to enable the partial reduction of Mn(IV) to Mn(III); accordingly, we used  $\text{MnO}_2$  (pyrolusite) as the precursor. CNFs and  $\text{MnO}_2$  were dispersed / dissolved in 10 M NaOH in a mass ratio of 30 to 70; other conditions of hydrothermal treatment were the same as those used for the synthesis of NMO nanowires. The XRD pattern of the product of the hydrothermal treatment with  $\text{MnO}_2$  precursor (NMO/CNF sample) is presented in Figure 4a; the results of the Rietveld quantitative phase analysis are given in Table 1 and also reported in the plot legend of Figure 4a, for ease of reference. According to the analysis, the carbon content of the hybrid was 19.3%. We also performed a DSC and TGA analysis of both H-NMO (without CNFs) and NMO/CNF, as shown in Figure 4b. At 600 °C, compared to that for H-NMO, a net mass loss of 22.1% was observed for the NMO/CNF sample and attributed to CNF burning. Overall, this value is in reasonably good agreement with the value derived from the Rietveld analysis. Furthermore, birnessite was formed during hydrothermal synthesis as a side product, in an amount of about 2.8% (Figure 4a) or possibly less, assuming that the TGA evaluation of carbon content is more reliable.



**Figure 4.** (a) Rietveld refinement (red dot symbols) of the XRD pattern (black line) of the NMO/CNF sample (see Table 1); the graph below (orange line) shows the discrepancy;  $R$  values:  $R_{wp} = 8.99\%$ ;  $R_p = 6.78\%$ ; goodness of fit:  $S = 1.24$ . (b) TGA and DSC curves of the hydrothermally grown NMO nanowires, H-NMO, and the NMO nanowire/CNF hybrid, NMO/CNF.

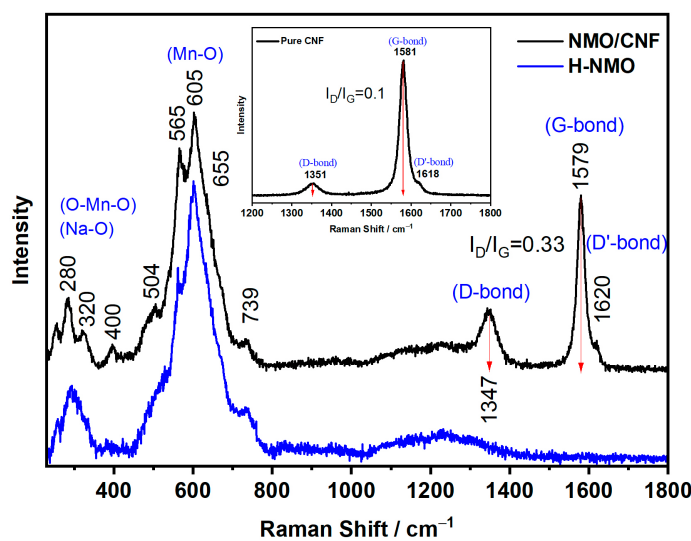
Overall, as we will show in more detail in the following, we devised a hydrothermal process using a  $\text{MnO}_2$  precursor for the preparation of an NMO nanowire/CNF hybrid with a significant reduction in the treatment time, from 3 days to 1 day, compared to that in the analogous synthesis of NMO nanowires based on  $\text{Mn}_2\text{O}_3$ . To the best of our knowledge, this is the first report demonstrating the preparation of an NMO/carbon hybrid using a hydrothermal method in a single day of treatment.

The structure and morphology of NMO/CNF was examined via SEM and TEM and the results are shown in Figure 5. Based on the SEM and TEM observations, it appears that the NMO nanowires synthesized via the  $\text{MnO}_2$  hydrothermal process were longer (having length of several tenths of  $\mu\text{m}$ , Figure 5a) and slightly thinner, with a width of about 50 nm (Figure 5b), having, then, a higher aspect ratio compared to that of the similar product obtained via  $\text{Mn}_2\text{O}_3$ -based synthesis (Figure 1d). Furthermore, a slightly lower tendency to grow in bundles may be inferred from Figure 5a compared to Figure 1d, though the bundles look thicker. CNFs are difficult to identify in FESEM images; however, nanofibers may be spotted in Figure 5a through their wider lateral size (about 100 nm) compared to that of NMO nanowires. Notably, a relatively large and thin platelet of birnessite can also be seen in the lower-left corner of Figure 5a. Eventually, TEM examination (Figure 5b) clearly showed the coexistence of CNFs and NMO nanowires in the sample, making the former distinguishable from the latter by the relatively high transparency and the larger width.



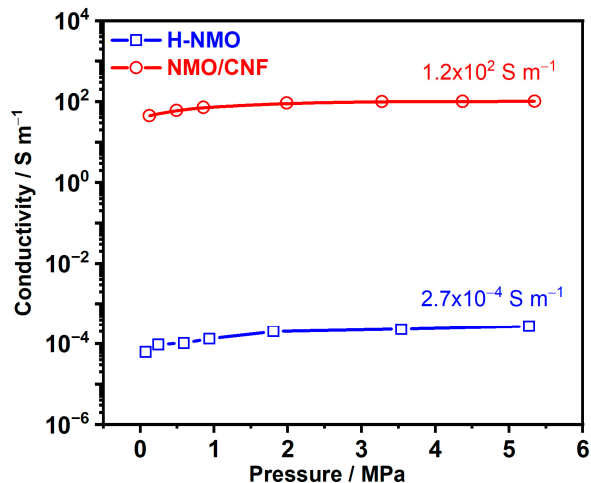
**Figure 5.** (a) Secondary SEM image of NMO/CNF sample; scale bar, 5  $\mu\text{m}$ . (b) Bright-field TEM image of NMO/CNF sample; scale bar, 200 nm.

Figure 6 shows the Raman spectra of H-NMO and NMO/CNF over the range of wavenumbers from 200 to 1800  $\text{cm}^{-1}$ . The vibration bands in the range 550–750  $\text{cm}^{-1}$  are associated with the stretching vibrations of Mn–O bonds and characterized by two distinct modes, at about 565 and 655  $\text{cm}^{-1}$  for both samples, which correspond to the stretching vibrations of  $\text{Mn}^{\text{IV}}\text{--O}$  and  $\text{Mn}^{\text{III}}\text{--O}$  bonds in  $\text{MnO}_6$  octahedrons and  $\text{MnO}_5$  square pyramids, respectively [58]. The lower-frequency bands (at 504, 400, 320 and 280  $\text{cm}^{-1}$  for NMO/CNF, shifted to slightly higher values for H-NMO) are attributed to the bending vibrations of Mn–O bonds and stretching vibrations of Na–O bonds [59,60]. Slight differences in the spectra of the as-grown H-NMO compared to those of NMO/CNF, i.e., the lower intensity of the stretching vibration of the  $\text{Mn}^{\text{IV}}\text{--O}$  band at about 565  $\text{cm}^{-1}$  and the broadening of low-frequency bands, indicate the slightly lower crystallinity and relatively higher defect concentration of the H-NMO sample. Finally, the carbon-related bands detected at 1347, 1579, and 1620  $\text{cm}^{-1}$  are attributed to disordered and defective carbon bonds (D and D') and graphitic carbon bonds (G). The intensity ratio of the D to G band ( $I_{\text{D}}/I_{\text{G}}$ ) is commonly used to measure the degree of defects in carbon materials [46]. The  $I_{\text{D}}/I_{\text{G}}$  of as-received CNFs was estimated to be about 0.1 (spectrum shown in the inset of Figure 6); in the hybrid product, the ratio increased to 0.33, thus suggesting an increase in surface disorder (higher defect number) of the carbon fibers during the hydrothermal treatment.



**Figure 6.** Raman spectra of H-NMO and NMO/CNF samples, and, in the inset, of pure CNFs.

Lastly, for the practical assessment of the NMO/CNF hybrid, we measured the electrical conductivity of the powder products. The measured conductivity of H-NMO and NMO/CNF samples is plotted in Figure 7 as a function of the compaction pressure showing a well-defined plateau with increasing pressure above about 2 MPa. There is a difference of almost six orders of magnitude between the plateau values of the conductivity of the two samples. This will have a strong effect on the rate performance of the electrode, as reported in the following section.



**Figure 7.** Electrical conductivity of the hydrothermally grown NMO nanowires, H-NMO, and the NMO nanowire/CNF hybrid, NMO/CNF, as a function of compaction pressure.

### 3.2. Electrochemical Study of H-NMO and NMO/CNF Electrodes

#### 3.2.1. Cyclic Voltammetry

The CV curves measured for the H-NMO and NMO/CNF electrodes in the 1 M Na<sub>2</sub>SO<sub>4</sub> solution are plotted in Figure 8; the electrodes were cycled five times in a range of potential from 0.25 to 1 V at a scan rate of 0.2 mV s<sup>-1</sup>. There was a very good overlap between successive cycles, the only noticeable difference being the slight increase in the peak current for the NMO/CNF electrode. The overall shape and the main features of the CV curves are consistent with those reported in previous studies [14,15,28]; in particular, the peaks in CV correspond to the de-/intercalation of Na ions in the NMO host structure from/into different sites (in S-shaped channels), as inferred from compositional and structural modifications [15,24,53]. For a detailed study of the CV behavior of the

NMO-based electrode in 1 M  $\text{Na}_2\text{SO}_4$ , we refer to our previous work [15], where it was shown, in particular, that the  $x$  composition in  $\text{Na}_x\text{MnO}_2$  varies between 0.40 and 0.22 over the potential range from 0.25 to 1.0 V; correspondingly, the theoretical capacity of NMO in this potential range is about 50 mAh g<sup>-1</sup>.

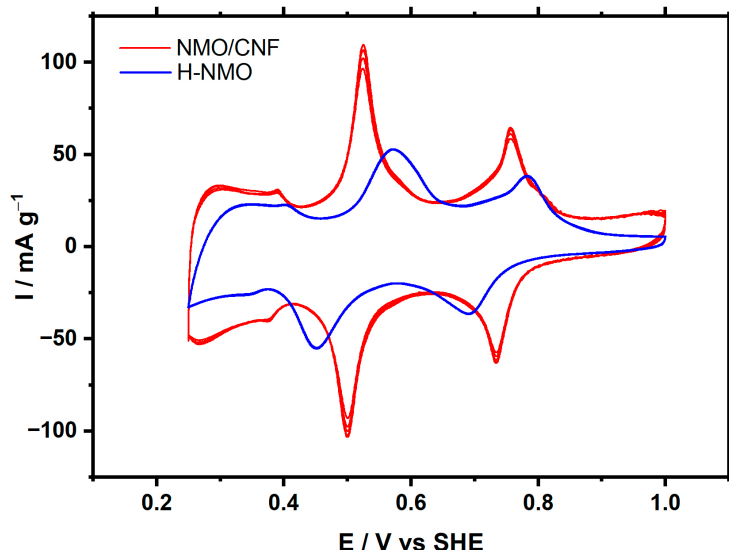


**Figure 8.** First five CV cycles of H-NMO and NMO/CNF electrodes at 0.2 mV s<sup>-1</sup> in the 1 M  $\text{Na}_2\text{SO}_4$  solution. Successive cycles are very similar to each other and then barely distinguishable.

Apart from the general features, there are two obvious differences in the CV curves of H-NMO and NMO/CNF electrodes: the peaks are sharper and the peak current is much higher for NMO/CNF compared to those of the H-NMO electrode; the distance between deintercalation and intercalation peaks is much smaller for NMO/CNF (~25 mV) compared to that for the H-NMO electrode (~120 and ~95 mV, for peak couples at a mean potential of 0.51 V and 0.74 V, respectively). Such a small peak potential gap is indicative of the kinetic reversibility of the de/embedding process of NMO/CNF electrodes. Noteworthily, the reversible character of the CV response of the NMO/CNF electrode was observed at a scan rate (0.2 mV s<sup>-1</sup>) relatively high compared to electrodes based on NMO formed via solid state synthesis with 22% CC (the same content of the H-NMO electrode); in fact, for the latter, a comparable potential gap—namely, about 30 mV—between de/embedding peaks was observed at a scan rate of 0.05 mV s<sup>-1</sup> [15].

Overall, given the comparable content of the conductive component in the electrode paste (~22% of CC or CNFs), the clear and strong difference in the CV response of H-NMO and the NMO/CNF electrode finds its explanation in the effective operation of CNFs as a distributed interconnection network in the electrode.

### 3.2.2. Galvanostatic Charge and Discharge Test

GCD tests were performed on the H-NMO and NMO/CNF electrodes at varying C-rates in the range from C/10 to 20 C. For each C-rate value, we recorded at least 10 GCD cycles, and the 10th cycle is the charge and discharge profile plotted in Figure 9a. The profile's shape is consistent with that of previous studies on NMO-based electrodes in an aqueous  $\text{Na}_2\text{SO}_4$  electrolyte; see [14,32] and the supplementary material of Ref. [15]. As shown in Figure 9b, the H-NMO and NMO/CNF samples display a similar capacity retention of up to C/2; at higher C-rates, the NMO/CNF electrode shows improved rate performance, with more than half of the theoretical capacity being maintained at the high rate of 20 C (1000 mA g<sup>-1</sup>), while the capacity of the H-NMO electrode is reduced to almost zero already at C-rate of 10 C. After 200 cycles at a C-rate of 2, and 200 more cycles at a C-rate of 10, see Figure 9c, the capacity of NMO/CNF remained reasonably stable, with a coulombic efficiency close to 100% at 2 C and about 98% at 10 C. This

demonstrates the good electrochemical stability of the NMO/CNF electrode at high C-rate values, which makes it suitable for use in supercapacitor–battery hybrids [61]. However, there is a small loss of capacity upon cycling at a high rate, 10 C, as revealed by the slow decaying trend of coulombic efficiency, from about 99% to 98%, under 200 cycles (Figure 9c). Additionally, after 10 cycles at 20 C, the capacity observed at C/2 is slightly reduced (Figure 9b), presumably due to a small loss of the active material via the irreversible modification of the electrode at this high rate. Still, this effect is slightly more pronounced for the H-NMO electrode (Figure 9b).

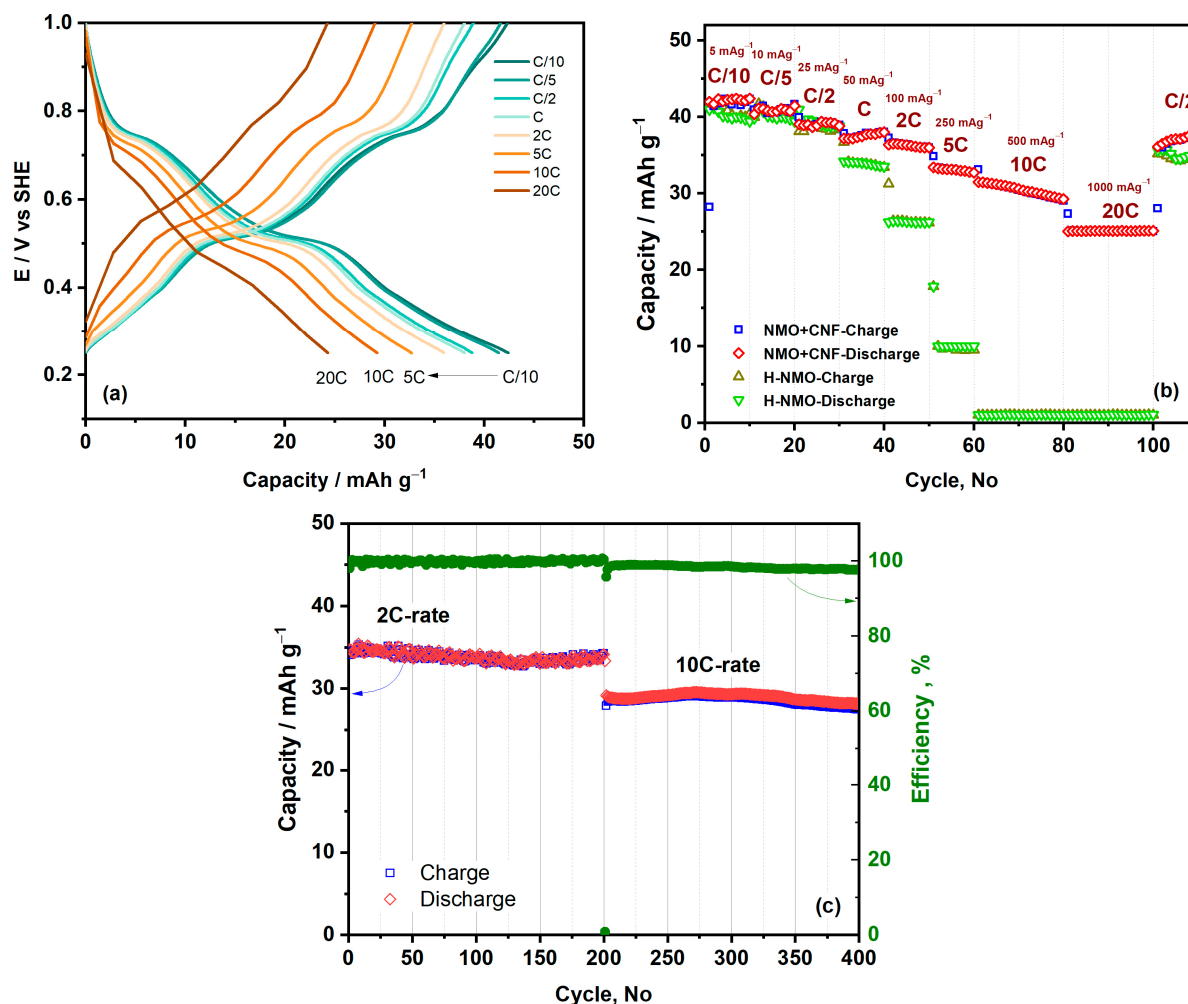


**Figure 9.** (a) Tenth charge and discharge profile of NMO/CNF at a C/10 to 20 C rate; (b) rate capability of H-NMO and NMO/CNF,  $1\text{C} \cong 50 \text{ mAh g}^{-1}$  [15]; (c) long-term charge and discharge of NMO/CNF at 2 C and 10 C rates.

Another point worth noticing is the fact that both NMO/CNF and H-NMO electrodes show a capacity below the theoretical value, which is about  $50 \text{ mAh g}^{-1}$ . Most notably, in accord with the above discussion underlining the reversible kinetics of the CNF/NMO electrode under CV at  $0.2 \text{ mV s}^{-1}$ , we would expect this electrode to achieve a close-to-theoretical capacity at a low-enough C-rate, such as C/10 [15], whereas instead the capacity is less than 90% of the theoretical value. The H-NMO electrode reveals a similar trend and a slightly lower capacity at C/10. The above observations of the morphology of the nanowires produced via either the  $\text{Mn}_2\text{O}_3$  or  $\text{MnO}_2$  hydrothermal method may give insight into this behavior; namely, we surmise that the lower than theoretical capacity is the result of nanowire bunching, which may prevent direct contact between conductive fibers and the active material, and then attribute the electron transport to NMO/NMO

contact. The fact that both electrodes reveal such a loss of capacity, with minimal difference, corroborates the hypothesis that nanowire bunching may be the origin of the effect, considering the observed formation of bundles in the hydrothermal products, albeit with some differences; see Sections 3.1.1 and 3.1.2. This issue calls for a more in-depth study on synthesis as well as on the electrode fabrication process.

Nonetheless, the strong difference in the galvanostatic charge–discharge response between H-NMO and NMO/CNF electrodes is apparent; even though the addition of CC improves the conductivity of the H-NMO electrode, its different morphology and, possibly, hardly homogeneous dispersion with nanowires are most likely the reasons why the CC particles result in a relatively poor electrical connection of NMO nanowires. Conversely, the mutual dispersion of CNFs and NMO nanowires, sharing a similar morphology and a comparable high aspect ratio, is able to ensure the formation of a distributed contact network and an effective connection. As a result, the incorporation of CNFs leads to a marked reduction in the electrode resistance and to a higher capacity at a high rate, with the attendant enhancement of cycling and power performance, with respect to the H-NMO electrode.

### 3.2.3. Electrochemical Impedance Spectroscopy

Figure 10 shows the complex plots of the two electrodes measured at OCP. The lower overall resistance of the NMO/CNF electrode compared to that of the H-NMO electrode is evident in the graphs. Both plots were fitted using the equivalent circuit (EC) shown in the inset of Figure 10, which we first proposed in Ref. [15] for the simulation of the impedance spectra of the solid-state synthesis of NMO electrodes in the 1 M Na<sub>2</sub>SO<sub>4</sub> solution, to study the contribution of different charging processes to charge storage.

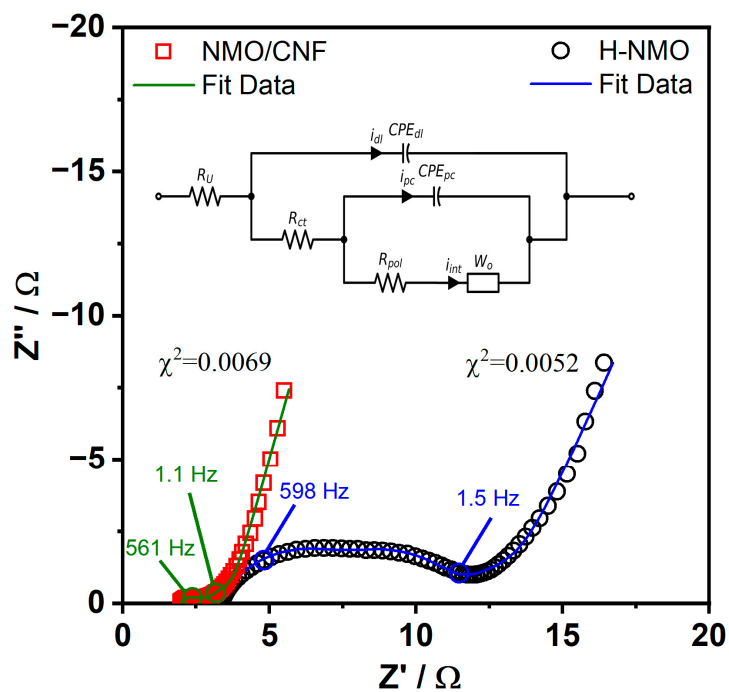


**Figure 10.** Nyquist plots of the impedance of H-NMO (empty circle symbol) and NMO/CNF (empty rectangle symbol) electrodes at OCP; solid lines represent the fit of the equivalent circuit model (in the inset) to the experimental data.

In the EC model,  $R_U$  stands for the combined resistance of the electrolyte and electrode, including the contact resistance at the electrode–current collector interface;  $R_{ct}$  is the charge transfer resistance of surface redox processes leading to charge storage via the pseudocapacitance represented by  $CPE_{pc}$  (constant phase element),  $CPE_{pc}$ ; analogously,  $CPE_{dl}$  stands for the interface capacitance and accounts for double-layer charge storage.

CPE impedance is defined as  $Z = 1/(q_0(j\omega)^n)$ , where  $q_0$  is the CPE capacitance parameter, in  $\Omega^{-1} s^n$ , and  $n$  is the dimensionless exponent that varying between 0 and 1 gives the phase value of  $(-90 \times n)^\circ$ .  $R_{pol}$  is the resistance related to the transfer of Na ions from/to the host crystal to/from the surface;  $W_o$  is the Na ion bounded diffusion impedance, modeled with the Warburg open element [62], expressed as  $W_o = W_R (j\omega W_T)^p \coth[(j\omega W_T)^p]$ , where the  $p$  exponent allows for anomalous diffusion, and  $W_R$  and  $W_T$  are the Warburg coefficient and the time constant of the diffusion model, respectively [63,64]. As shown in Figure 10, the fit was good and acceptable, as evidenced by the low chi-squared,  $\chi^2$ , values. The fitted values of the EC model for both electrodes are given in Table 2. All the resistance parameters,  $R_U$ ,  $R_{pol}$  and  $W_R$ , are significantly lower for the NMO/CNF electrode compared to those for the H-NMO electrode, which is readily explained by the effective electrical wiring induced by the presence of CNFs. In addition, the interface capacitance and the pseudocapacitance of the NMO+CNF electrode are slightly higher. The interface capacitance is higher probably due to the higher active surface area of CNFs, compared to that of CC in the H-NMO electrode; the pseudocapacitance, in turn, increases in conjunction with the reduction in  $R_{ct}$ .

**Table 2.** Fitting parameters of the equivalent circuit model shown in the inset of Figure 10 for the EIS measurements of H-NMO and NMO/CNF electrodes at OCP in the 1 M  $\text{Na}_2\text{SO}_4$  solution.

	H-NMO		NMO/CNF	
Element	Value	Standard error	Value	Standard error
$R_U$ ( $\Omega$ )	3.345	0.006	1.976	0.0053
$R_{ct}$ ( $\Omega$ )	5.412	0.036	0.566	0.0167
$CPE_{dl}$ (F)	$0.769 \times 10^{-3}$	$6.088 \times 10^{-6}$	$1.9 \times 10^{-3}$	$8.6 \times 10^{-5}$
$n1$	0.75	-	0.75	-
$R_{pol}$ ( $\Omega$ )	2.246	0.040	0.1776	0.0146
$CPE_{pc}$ (F)	0.004	$2.003 \times 10^{-4}$	0.008	0.0014
$n2$	0.9	-	0.9	-
$W_R$ ( $\Omega$ )	6.893	0.265	2.608	0.0628
$W_T$ (s)	22.263	1.398	5.227	0.1844
$p$	0.372	0.0049	0.405	0.0019

#### 4. Conclusions

We devised a hydrothermal process using a  $\text{MnO}_2$  precursor for the preparation of a NMO nanowire/CNF hybrid within a single day of treatment. Electrodes based on the NMO/CNF hybrid (about a 22% carbon content from CNFs) showed a strong enhancement of rate capability compared to that of electrodes fabricated with NMO nanowires using a conventional electrode paste composition (22% CC content). The synthesis method and the similarity in morphology between CNFs and nanowires (of a width of about 50 nm and length of several tenths of  $\mu\text{m}$ ) reasonably allowed for a good dispersion of the hybrid components. The increase in conductivity of the NMO/CNF hybrid by several orders of magnitude compared to that of the NMO nanowires resulted in an exceptional improvement in rate performance. The NMO/CNF electrode was able to retain over 50% of its theoretical capacity at a C-rate of up to 20 C. Furthermore, the stability of the material was demonstrated after 400 cycles at a high C-rate, making it promising for use in Na-ion storage systems.

**Supplementary Materials:** The following supporting information can be downloaded at <https://www.mdpi.com/article/10.3390/batteries9080428/s1>. Figure S1: Rietveld refinement of the XRD pattern of the product of the synthesis step HT#1; Figure S2: Rietveld refinement of the XRD pattern of the product of the synthesis step HT#2; Figure S3: Comparison of XRD patterns of the product of the hydrothermal synthesis step HT#1 (labeled “after 1 day” in the plot legend) and of the product obtained in the same conditions but after 6 days of continuous treatment; Figure S4: Isotherm plot of the product of the hydrothermal synthesis step HT#3 (H-NMO sample); Figure S5: BET surface area plot of the product of the hydrothermal synthesis step HT#3 (H-NMO sample); Table S1: Summary of results obtained from linear fitting of BET plot.

**Author Contributions:** Conceptualization, M.S. and M.R.; data curation, M.S. and J.M.; formal analysis, M.S., J.M. and M.B.; funding acquisition, M.R. and A.V.; investigation, M.S., M.R. and J.M.; methodology, M.B. and A.V.; project administration, M.S. and M.R.; resources, M.R. and A.V.; supervision, A.V.; validation, M.S., M.R., J.M. and M.B.; visualization, M.S., M.R., J.M. and M.B.; writing—original draft, M.S.; writing—review and editing, A.V. All authors have read and agreed to the published version of the manuscript.

**Funding:** This work was funded by the Research Fund for the Italian Electrical System under the Three-Year Research Plan 2022–2024 (DM MITE n. 337, 15.09.2022), in compliance with the Decree of 16 April 2018.

**Data Availability Statement:** Data will be made available on request.

**Conflicts of Interest:** The authors declare no conflict of interest. The funders had no role in the design of the study; in the collection, analyses, or interpretation of data; in the writing of the manuscript; or in the decision to publish the results.

## References

1. Kim, H.; Hong, J.; Park, K.-Y.; Kim, H.; Kim, S.-W.; Kang, K. Aqueous Rechargeable Li and Na Ion Batteries. *Chem. Rev.* **2014**, *114*, 11788–11827. [[CrossRef](#)]
2. Bin, D.; Wang, F.; Tamirat, A.G.; Suo, L.; Wang, Y.; Wang, C.; Xia, Y. Progress in Aqueous Rechargeable Sodium-Ion Batteries. *Adv. Energy Mater.* **2018**, *8*, 1–31. [[CrossRef](#)]
3. Yang, M.; Luo, J.; Guo, X.; Chen, J.; Cao, Y.; Chen, W. Review Aqueous Rechargeable Sodium-Ion Batteries: From Liquid to Hydrogel. *Batteries* **2022**, *8*, 180. [[CrossRef](#)]
4. Boyd, S.; Augustyn, V. Transition metal oxides for aqueous sodium-ion electrochemical energy storage. *Inorg. Chem. Front.* **2018**, *5*, 999–1015. [[CrossRef](#)]
5. Mauger, A.; Julien, C.M. State-of-the-Art Electrode Materials for Sodium-Ion Batteries. *Materials* **2020**, *13*, 3453. [[CrossRef](#)] [[PubMed](#)]
6. Liu, Q.; Hu, Z.; Chen, M.; Zou, C.; Jin, H.; Wang, S.; Chou, S.-L.; Liu, Y.; Dou, S.-X. The Cathode Choice for Commercialization of Sodium-Ion Batteries: Layered Transition Metal Oxides versus Prussian Blue Analogs. *Adv. Funct. Mater.* **2020**, *30*, 1909530. [[CrossRef](#)]
7. Wei, W.; Cui, X.; Chen, W.; Ivey, D.G. Manganese oxide-based materials as electrochemical supercapacitor electrodes. *Chem. Soc. Rev.* **2011**, *40*, 1697–1721. [[CrossRef](#)] [[PubMed](#)]
8. Gao, Y.; Yang, H.; Bai, Y.; Wu, C. Mn-based oxides for aqueous rechargeable metal ion batteries. *J. Mater. Chem. A* **2021**, *9*, 11472–11500. [[CrossRef](#)]
9. Shin, J.; Seo, J.K.; Yaylian, R.; Huang, A.; Meng, Y.S. A review on mechanistic understanding of MnO<sub>2</sub> in aqueous electrolyte for electrical energy storage systems. *Int. Mater. Rev.* **2020**, *65*, 356–387. [[CrossRef](#)]
10. Arias, N.P.; Becerra, M.E.; Giraldo, O. Structural and Electrical Studies for Birnessite-Type Materials Synthesized by Solid-State Reactions. *Nanomaterials* **2019**, *9*, 1156. [[CrossRef](#)]
11. Siamionau, U.; Aniskevich, Y.; Mazanik, A.; Kokits, O.; Ragoisha, G.; Jo, J.H.; Myung, S.-T.; Streltsov, E. Rechargeable zinc-ion batteries with manganese dioxide cathode: How critical is choice of manganese dioxide polymorphs in aqueous solutions? *J. Power Sources* **2022**, *523*, 231023. [[CrossRef](#)]
12. Li, H.; Zhang, W.; Sun, K.; Guo, J.; Yuan, K.; Fu, J.; Zhang, T.; Zhang, X.; Long, H.; Zhang, Z.; et al. Manganese-Based Materials for Rechargeable Batteries beyond Lithium-Ion. *Adv. Energy Mater.* **2021**, *11*, 2100867. [[CrossRef](#)]
13. Chae, M.S.; Elias, Y.; Aurbach, D. Tunnel-type sodium manganese oxide cathodes for sodium-ion batteries. *ChemElectroChem* **2021**, *8*, 798–811. [[CrossRef](#)]
14. Whitacre, J.F.; Tevar, A.; Sharma, S. Na<sub>4</sub>Mn<sub>9</sub>O<sub>18</sub> as a positive electrode material for an aqueous electrolyte sodium-ion energy storage device. *Electrochim. Commun.* **2010**, *12*, 463–466. [[CrossRef](#)]
15. Soleimanzade, M.; Bahdanchyk, M.; Hashempour, M.; Bestetti, M.; Cernuschi, F.M.; Vicenzo, A. Charging processes of Na<sub>4</sub>Mn<sub>9</sub>O<sub>18</sub> electrode in aqueous electrolyte. *Electrochim. Acta* **2022**, *426*, 140791. [[CrossRef](#)]
16. Kim, H.; Kim, D.J.; Seo, D.H.; Yeom, M.S.; Kang, K.; Kim, D.K.; Jung, Y. Ab initio study of the sodium intercalation and intermediate phases in Na<sub>0.44</sub>MnO<sub>2</sub> for sodium-ion battery. *Chem. Mater.* **2012**, *24*, 1205–1211. [[CrossRef](#)]
17. Sauvage, F.; Baudrin, E.; Tarascon, J.M. Study of the potentiometric response towards sodium ions of Na<sub>0.44-x</sub>MnO<sub>2</sub> for the development of selective sodium ion sensors. *Sens. Actuators B* **2007**, *120*, 638–644. [[CrossRef](#)]
18. Clément, R.J.; Bruce, P.G.; Grey, C.P. Review—Manganese-Based P2-Type Transition Metal Oxides as Sodium-Ion Battery Cathode Materials. *J. Electrochem. Soc.* **2015**, *162*, A2589. [[CrossRef](#)]
19. Zuo, W.; Innocenti, A.; Zarrabeitia, M.; Bresser, D.; Yang, Y.; Passerini, S. Layered Oxide Cathodes for Sodium-Ion Batteries: Storage Mechanism, Electrochemistry, and Techno-economics. *Acc. Chem. Res.* **2023**, *56*, 284–296. [[CrossRef](#)]
20. Zhang, H.; Liu, X.; Li, H.; Hasa, I.; Passerini, S. Challenges and Strategies for High-Energy Aqueous Electrolyte Rechargeable Batteries. *Angew. Chem. Int. Ed.* **2021**, *60*, 598–616. [[CrossRef](#)]

21. Yang, Z.; Zhang, J.; Kintner-Meyer, M.C.W.; Lu, X.; Choi, D.; Lemmon, J.P.; Liu, J. Electrochemical Energy Storage for Green Grid. *Chem. Rev.* **2011**, *111*, 3577–3613. [CrossRef] [PubMed]
22. Chen, Z.; Yuan, T.; Pu, X.; Yang, H.; Ai, X.; Xia, Y.; Cao, Y. Symmetric Sodium-Ion Capacitor Based on  $\text{Na}_{0.44}\text{MnO}_2$  Nanorods for Low-Cost and High-Performance Energy Storage. *ACS Appl. Mater. Interfaces* **2018**, *10*, 11689–11698. [CrossRef]
23. Parant, J.P.; Olazcuaga, R.; Devalette, M.; Fouassier, C.; Hagenmuller, P. Sur quelques nouvelles phases de formule  $\text{Na}_x\text{MnO}_2$  ( $x \leq 1$ ). *J. Solid State Chem.* **1971**, *3*, 1–11. [CrossRef]
24. Sauvage, F.; Laffont, L.; Tarascon, J.M.; Baudrin, E. Study of the insertion/deinsertion mechanism of sodium into  $\text{Na}_{0.44}\text{MnO}_2$ . *Inorg. Chem.* **2007**, *46*, 3289–3294. [CrossRef]
25. He, X.; Wang, J.; Qiu, B.; Paillard, E.; Ma, C.; Cao, X.; Liu, H.; Stan, M.C.; Liu, H.; Gallash, T.; et al. Durable high-rate capability  $\text{Na}_{0.44}\text{MnO}_2$  cathode material for sodium-ion batteries. *Nano Energy* **2016**, *27*, 602–610. [CrossRef]
26. Caballero, A.; Hernán, L.; Morales, J.; Sánchez, L.; Santos Peña, J.; Aranda, M.A.G. Synthesis and characterization of high-temperature hexagonal P2- $\text{Na}_{0.6}\text{MnO}_2$  and its electrochemical behaviour as cathode in sodium cells. *J. Mater. Chem.* **2002**, *12*, 1142–1147. [CrossRef]
27. Zuo, W.; Yang, Y. Synthesis, Structure, Electrochemical Mechanisms, and Atmospheric Stability of Mn-Based Layered Oxide Cathodes for Sodium Ion Batteries. *Acc. Mater. Res.* **2022**, *3*, 709–720. [CrossRef]
28. Kim, D.J.; Ponraj, R.; Kannan, A.G.; Lee, H.W.; Fathi, R.; Ruffo, R.; Mari, C.M.; Kim, D.K. Diffusion behavior of sodium ions in  $\text{Na}_{0.44}\text{MnO}_2$  in aqueous and non-aqueous electrolytes. *J. Power Sources* **2013**, *244*, 758–763. [CrossRef]
29. Nitta, N.; Wu, F.; Lee, J.T.; Yushin, G. Li-ion battery materials: Present and future. *Mater. Today* **2015**, *18*, 252–264. [CrossRef]
30. Bruce, P.G.; Scrosati, B.; Tarascon, J.-M. Nanomaterials for Rechargeable Lithium Batteries. *Angew. Chem. Int. Ed.* **2008**, *47*, 2930–2946. [CrossRef]
31. Fang, Y.; Yu, X.-Y.; Lou, X.W.D. Nanostructured Electrode Materials for Advanced Sodium-Ion Batteries. *Matter* **2019**, *1*, 90–114. [CrossRef]
32. Zhou, X.; Zhao, A.; Chen, Z.; Cao, Y. Research progress of tunnel-structural  $\text{Na}_{0.44}\text{MnO}_2$  cathode for sodium-ion batteries: A mini review. *Electrochim. Commun.* **2021**, *122*, 106897. [CrossRef]
33. Li, Y.; Wu, Y. Formation of  $\text{Na}_{0.44}\text{MnO}_2$  nanowires via stress-induced splitting of birnessite nanosheets. *Nano Res.* **2009**, *2*, 54–60. [CrossRef]
34. Park, Y.; Woo Lee, S.; Kim, K.H.; Min, B.K.; Kumar Nayak, A.; Pradhan, D.; Sohn, Y. Understanding hydrothermal transformation from  $\text{Mn}_2\text{O}_3$  particles to  $\text{Na}_{0.55}\text{Mn}_2\text{O}_4 \cdot 1.5\text{H}_2\text{O}$  nanosheets, nanobelts, and single crystalline ultra-long  $\text{Na}_4\text{Mn}_9\text{O}_{18}$  nanowires. *Sci. Rep.* **2015**, *5*, 18275. [CrossRef] [PubMed]
35. Hosono, E.; Matsuda, H.; Honma, I.; Fujihara, S.; Ichihara, M.; Zhou, H. Synthesis of single crystalline electro-conductive  $\text{Na}_{0.44}\text{MnO}_2$  nanowires with high aspect ratio for the fast charge–discharge Li ion battery. *J. Power Sources* **2008**, *182*, 349–352. [CrossRef]
36. Cao, Y.L.; Xiao, L.F.; Wang, W.; Choi, D.W.; Nie, Z.M.; Yu, J.G.; Saraf, L.V.; Yang, Z.G.; Liu, J. Reversible Sodium Ion Insertion in Single Crystalline Manganese Oxide Nanowires with Long Cycle Life. *Adv. Mater.* **2011**, *23*, 3155–3160. [CrossRef]
37. Kim, J.; Choi, M.S.; Shin, K.H.; Kota, M.; Kang, Y.; Lee, S.; Lee, J.Y.; Park, H.S. Rational Design of Carbon Nanomaterials for Electrochemical Sodium Storage and Capture. *Adv. Mater.* **2019**, *31*, 1803444. [CrossRef]
38. Zhao, L.; Ni, J.; Wang, H.; Gao, L.  $\text{Na}_{0.44}\text{MnO}_2$ -CNT electrodes for non-aqueous sodium batteries. *RSC Adv.* **2013**, *3*, 6650. [CrossRef]
39. Li, Z.; Young, D.; Xiang, K.; Carter, W.C.; Chiang, Y.M. Towards high power high energy aqueous sodium-ion batteries: The  $\text{NaTi}_2(\text{PO}_4)_3/\text{Na}_{0.44}\text{MnO}_2$  system. *Adv. Energy Mater.* **2013**, *3*, 290–294. [CrossRef]
40. Gu, F.; Sun, T.; Yao, X.; Shui, M.; Shu, J. Studies on the improved electrochemical performance and the sodium ion migration mechanism of  $\text{Na}_{0.44}\text{MnO}_2$ -CNT electrodes for aqueous sodium batteries. *J. Phys. Chem. Solids* **2021**, *149*, 109771. [CrossRef]
41. Guo, Z.; Zhao, Y.; Ding, Y.; Dong, X.; Chen, L.; Cao, J.; Wang, C.; Xia, Y.; Peng, H.; Wang, Y. Multi-functional Flexible Aqueous Sodium-Ion Batteries with High Safety. *Chem* **2017**, *3*, 348–362. [CrossRef]
42. Yin, F.; Liu, Z.; Yang, S.; Shan, Z.; Zhao, Y.; Feng, Y.; Zhang, C.; Bakenov, Z.  $\text{Na}_4\text{Mn}_9\text{O}_{18}$ /Carbon Nanotube Composite as a High Electrochemical Performance Material for Aqueous Sodium-Ion Batteries. *Nanoscale Res. Lett.* **2017**, *12*, 569. [CrossRef] [PubMed]
43. Lu, D.; Yao, Z.; Zhong, Y.; Wang, X.; Xia, X.; Gu, C.; Wu, J.; Tu, J. Polypyrrole-Coated Sodium Manganate Hollow Microspheres as a Superior Cathode for Sodium Ion Batteries. *ACS Appl. Mater. Interfaces* **2019**, *11*, 15630–15637. [CrossRef]
44. Lu, D.; Yao, Z.J.; Li, Y.Q.; Zhong, Y.; Wang, X.L.; Xie, D.; Xia, X.H.; Gu, C.D.; Tu, J.P. Sodium-rich manganese oxide porous microcubes with polypyrrole coating as a superior cathode for sodium ion full batteries. *J. Colloid Interface Sci.* **2020**, *565*, 218–226. [CrossRef] [PubMed]
45. Akimoto, J.; Hayakawa, H.; Kijima, N.; Awaka, J.; Funabiki, F. Single-crystal synthesis and structure refinement of  $\text{Na}_{0.44}\text{MnO}_2$ . *Solid State Phenom.* **2011**, *170*, 198–202.
46. Coelho, A.A. TOPAS and TOPAS-Academic: An optimization program integrating computer algebra and crystallographic objects written in C++. *J. Appl. Crystallogr.* **2018**, *51*, 210–218. [CrossRef]
47. Toby, B. R factors in Rietveld analysis: How good is good enough? *Powder Diffr.* **2006**, *21*, 67–70. [CrossRef]
48. Mohseni-Salehi, M.S.; Taheri-Nassaj, E.; Babaei, A.; Soleimanzade, M. Effect of different precursors on the formation and physical properties of V2AlC MAX phase. *J. Alloys Compd.* **2022**, *918*, 165588. [CrossRef]

49. Hashempour, M.; Vicenzo, A.; Bahdanchyk, M.; Bestetti, M. Parameters influencing the capacitive behavior of carbon composite electrodes: Composition, morphology, electrical conductivity, and surface chemistry. *J. Solid State Electrochem.* **2018**, *22*, 3895–3911. [[CrossRef](#)]
50. Bahdanchyk, M.; Hashempour, M.; Vicenzo, A. Evaluation of the operating potential window of electrochemical capacitors. *Electrochim. Acta* **2020**, *332*, 135503. [[CrossRef](#)]
51. Boukamp, B.A. A Linear Kronig-Kramers Transform Test for Immittance Data Validation. *J. Electrochem. Soc.* **1995**, *142*, 1885–1894. [[CrossRef](#)]
52. Soleimanzade, M. Sodium Manganese Oxide Cathode towards the Development of Aqueous Sodium Ion Storage Devices. Ph.D. Thesis, Politecnico di Milano, Milan, Italy, 2021.
53. Chu, Q.; Wang, X.; Li, Q.; Liu, X. The tunnel manganese oxide  $\text{Na}_{4.32}\text{Mn}_9\text{O}_{18}$ : A new  $\text{Na}^+$  site discovered by single-crystal X-ray diffraction. *Acta Crystallogr. Sect. C* **2011**, *67*, i10–i12. [[CrossRef](#)] [[PubMed](#)]
54. Davies, G. Some aspects of the chemistry of manganese(III) in aqueous solution. *Coord. Chem. Rev.* **1969**, *4*, 199–224. [[CrossRef](#)]
55. Liu, L.; Feng, Q.; Yanagisawa, K.; Wang, Y. Characterization of birnessite-type sodium manganese oxides prepared by hydrothermal reaction process. *J. Mater. Sci. Lett.* **2000**, *19*, 2047–2050. [[CrossRef](#)]
56. Xia, G.-G.; Tong, W.; Tolentino, E.N.; Duan, N.-G.; Brock, S.L.; Wang, J.-Y.; Suib, S.L.; Ressler, T. Synthesis and characterization of nanofibrous sodium manganese oxide with a  $2 \times 4$  tunnel structure. *Chem. Mater.* **2001**, *13*, 1585–1592. [[CrossRef](#)]
57. Lanson, B.; Drits, V.A.; Feng, Q.; Manceau, A. Structure of synthetic Na-birnessite: Evidence for a triclinic one-layer unit cell. *Am. Mineral.* **2002**, *87*, 1662–1671. [[CrossRef](#)]
58. Huynh, L.T.; Vu, T.P.; Nguyen, V.H.; Phung Le, M.L.; Tran, V.M. Li-insertion into sol-gel  $\text{Na}_{0.44}\text{MnO}_2$  cathode material for higher structure and electrochemical performance of batteries. *Energy Storage* **2020**, *2*, e121. [[CrossRef](#)]
59. Julien, C.; Massot, M.; Rangan, S.; Lemal, M.; Guyomard, D. Study of structural defects in  $\gamma\text{-MnO}_2$  by Raman spectroscopy. *J. Raman Spectrosc.* **2002**, *33*, 223–228. [[CrossRef](#)]
60. Hardwick, L.J.; Saint, J.A.; Lucas, I.T.; Doeuff, M.M.; Kostecki, R. FTIR and Raman Study of the  $\text{Li}_x\text{Ti}_y\text{Mn}_{1-y}\text{O}_2$  ( $y = 0, 0.11$ ) Cathodes in Methylpropyl Pyrrolidinium Bis(fluoro-sulfonyl)imide, LiTFSI Electrolyte. *J. Electrochem. Soc.* **2009**, *156*, A120. [[CrossRef](#)]
61. Xing, F.; Bi, Z.; Su, F.; Liu, F.; Wu, Z.-S. Unraveling the Design Principles of Battery-Supercapacitor Hybrid Devices: From Fundamental Mechanisms to Microstructure Engineering and Challenging Perspectives. *Adv. Energy Mater.* **2022**, *12*, 2200594. [[CrossRef](#)]
62. Bisquert, J.; Compte, A. Theory of the electrochemical impedance of anomalous diffusion. *J. Electroanal. Chem.* **2001**, *499*, 112–120. [[CrossRef](#)]
63. Ho, C.; Raistrick, I.D.; Huggins, R.A. Application of A-C Techniques to the Study of Lithium Diffusion in Tungsten Trioxide Thin Films. *J. Electrochem. Soc.* **1980**, *127*, 343–350. [[CrossRef](#)]
64. Mohseni-Salehi, M.S.; Taheri-Nassaj, E.; Babaei, A.; Ghazvini, A.S.; Soleimanzade, M. Effect of temperature and atmosphere on  $\text{V}_2\text{AlC}$  etching for  $\text{V}_2\text{CT}_x$  MXenes synthesis used as anode for Li-ion storage systems. *J. Energy Storage* **2023**, *66*, 107462. [[CrossRef](#)]

**Disclaimer/Publisher's Note:** The statements, opinions and data contained in all publications are solely those of the individual author(s) and contributor(s) and not of MDPI and/or the editor(s). MDPI and/or the editor(s) disclaim responsibility for any injury to people or property resulting from any ideas, methods, instructions or products referred to in the content.